Theoret. Comput. Fluid Dynamics (2002) 16: 115–131
Digital Object Identifier (DOI) 10.1007/s00162-002-0073-x

Theoretical and Computational Fluid Dynamics

Flow Bifurcations in a Thin Gap Between Two Rotating Spheres

R.-J. Yang and W.-J. Luo

Department of Engineering Science,
National Cheng Kung University,
Tainan, Taiwan 70101, R.O.C.

Communicated by M.Y. Hussaini

Received 26 November 2001 and accepted 10 May 2002
Published online 30 October 2002 – © Springer-Verlag 2002

Abstract. This paper presents the use of a parameter continuation method and a test function to solve the steady, axisymmetric incompressible Navier–Stokes equations for spherical Couette flow in a thin gap between two concentric, differentially rotating spheres. The study focuses principally on the prediction of multiple steady flow patterns and the construction of bifurcation diagrams. Linear stability analysis is conducted to determine whether or not the computed steady flow solutions are stable. In the case of a rotating inner sphere and a stationary outer sphere, a new unstable solution branch with two asymmetric vortex pairs is identified near the point of a symmetry-breaking pitchfork bifurcation which occurs at a Reynolds number equal to 789. This solution transforms smoothly into an unstable asymmetric 1-vortex solution as the Reynolds number increases. Another new pair of unstable 2-vortex flow modes whose solution branches are unconnected to previously known branches is calculated by the present two-parameter continuation method. In the case of two rotating spheres, the range of existence in the $(Re_1,\ Re_2)$ plane of the one and two vortex states, the vortex sizes as a function of both Reynolds numbers are identified. Bifurcation theory is used to discuss the origin of the calculated flow modes. Parameter continuation indicates that the stable states are accompanied by certain unstable states.

1. Introduction

Spherical Couette flow, which occurs in flows through a thin gap between differentially rotating spheres, is known to possess multiple steady flow patterns. Wimmer (1976) investigated the case of a flow between a rotating inner and a stationary outer sphere with a gap width of $\sigma = 0.18$ (where $\sigma = (R_2 - R_1)/R_1$, and R_1 and R_2 are the radii of the inner and the outer spheres, respectively). He observed non-unique flow modes at a supercritical Reynolds number (i.e. $Re_1 = \omega_1 R_1^2/\nu$, where ω_1 represents the angular velocity of the inner rotating sphere, and ν is the kinematic viscosity), namely three steady axisymmetric modes and two unsteady non-axisymmetric modes. Steady modes contain either none, one, or two vortices per hemisphere near the equator, and are referred to as Mode I, Mode III, or Mode IV, respectively. Unsteady modes contain either one or two vortices. Wimmer (1976) demonstrated that these flow modes were induced by different accelerations of the inner sphere, i.e. each mode occurred when the inner sphere was specially accelerated to a particular angular velocity which corresponded to certain critical values of the Reynolds number. It was found that each flow mode had its own particular region of existence at steady state.

Published literature, including Bartles (1982), Marcus and Tuckerman (1987), Schrauf (1986), Bühler (1990), Mamun and Tuckerman (1995), and Yang (1996), provides prediction methods for the three steady axisymmetric flow modes, and discusses flow mode transitions and bifurcation behaviors. The roles played by equator symmetry-breaking in the transition process and flow mode bifurcation are of particular interest. For the case of a rotating inner sphere and a stationary outer sphere with a gap width of $\sigma = 0.18$ and $Re_1 \leq 800$, Schrauf (1986) and Marcus and Tuckerman (1987) deduced the bifurcation structure of the axisymmetric spherical Couette flow, and identified four bifurcation points. The first point was a saddle-node bifurcation, which occurred at $Re_1 \approx 645$, and which formed a pair of 1-vortex branches; one stable and the other unstable. The second and third bifurcation points were two subcritical pitchfork bifurcations undergone by the main branch at $Re_1 \approx 652$ and $Re_1 \approx 775$, respectively. The main branch changed continuously from zero to two vortex states. By definition, each subcritical pitchfork bifurcation created pairs of unstable branches. The branches originating at $Re_1 \approx 652$ were found to terminate via a pitchfork bifurcation (i.e. the fourth bifurcation point) on the unstable 1-vortex branch for the range $645 < Re_1 < 652$. It would be reasonable to expect that the bifurcation which occurred at $Re_1 \approx 775$ would also be accompanied by the creation of a pair of unstable asymmetric branches, and in fact this solution was reported by Luo and Yang (1998). This present paper investigates this solution in greater detail.

Some scholars have studied bifurcations in flows generated by concentric, co-/counter-rotating spheres. Yavorskaya and Belyaev (1986) observed a variety of steady axisymmetric and three-dimensional traveling wave secondary regimes in the case of $\sigma = 0.11$. Zikanov (1996) used a numerical simulation approach to identify three different types of symmetry-breaking primary bifurcations of the basic equilibrium. For $\sigma = 0.11$, Yavorskaya *et al*. (1977, 1980) and Yavorskaya and Belyaev (1986) showed that the basic flow only transforms to 1-vortex flow within a restricted range of outer-sphere angular velocity, namely in the range $-920 < Re_2 < 1940$, where $Re_2 = \omega_2 R_2^2/\nu$. Within the range $1940 < Re_2 < 4290$, the primary bifurcation ceases to exhibit rotational symmetry and instead becomes a three-dimensional, azimuthally traveling wave flow with spiral vortices which originates at the equator. Counter-rotation of the boundary spheres in the range $-3350 < Re_2 < -920$ results initially in instability in the form of azimuthally traveling spirals whose spatial structures, however, differ significantly from those mentioned above. Taylor vortices occur at the stability limit of the basic flow, but only within a restricted range of outer-sphere angular velocity. However, the precise boundaries of the different flow modes are yet to be determined. Thus, the aim of this current paper is to investigate further the precise nature of flow between co-/counter-rotating spheres, and to construct bifurcation structures for various values of Re_1. The origin of the flow modes identified will be explained by reference to bifurcation theory. Although it is known that some of the flows described above are non-axisymmetric in nature at high Reynolds number, the current study focuses only upon low Reynolds number axisymmetric flows due to the limitations of the available computing facilities.

Schrauf (1986) applied the continuation method proposed by Keller (1977) to the steady axisymmetric Navier–Stokes equations in order to investigate the stability regions of different flow modes for the case of a gap of $\sigma = 0.18$ and with inner sphere rotation only. The present study extends his work to both co- and counter-rotating spheres. In previous studies of Taylor–Couette flow which adopted a continuation method, the singular points were indicated by a sign change of the Jacobian determinant. However, this study applies an alternative method, namely a test function proposed by Seydel (1988). Using this approach, the bifurcation locations are indicated by changes of the test function sign.

The remainder of this paper is as follows: Section 2 provides an outline of the calculation method, and briefly reviews linear stability theory. Section 3 presents and discusses the numerical results and diagrams. Finally, Section 4 draws some conclusions.

2. Governing Equations and Numerical Methods

We consider a flow of steady, incompressible Newtonian fluid contained between two concentric co-/counter-rotating spheres. The governing equations are written in the spherical coordinate system. Since axisymmetric flows are considered, stream function Ψ, vorticity function ξ, and angular velocity function

ϕ can be introduced as follows:

$$v^r(r,\ \theta) = \frac{1}{r\sin\theta}\frac{1}{r}\frac{\partial}{\partial\theta}\psi(r,\ \theta), \tag{1a}$$

$$v^\theta(r,\ \theta) = -\frac{1}{r\sin\theta}\frac{\partial}{\partial r}\psi(r,\ \theta), \tag{1b}$$

$$v^\phi(r,\ \theta) = \frac{1}{r\sin\theta}\phi(r,\ \theta), \tag{1c}$$

$$(\nabla\times v)^\phi = \frac{1}{r}\left[\frac{\partial}{\partial r}\left(rv^\theta\right) - \frac{\partial}{\partial\theta}v^r\right] = \frac{1}{r\sin\theta}\xi(r,\ \theta). \tag{1d}$$

Let the radius of the inner sphere R_1 and angular velocity ω_1 be reference values of radius and angular velocity, respectively. Then non-dimensional quantities (denoted by asterisks) can be defined via

$$r = r^* R_1, \qquad u = u^* R_1\omega_1, \qquad \psi = \psi^* R_1^3\omega_1, \qquad \phi = \phi^* R_1^2\omega_1, \qquad \xi = \xi^* R_1\omega_1.$$

We drop the asterisks in the following sections, and the dimensionless momentum equation in the circumferential direction is

$$\frac{\partial\psi}{\partial\theta}\frac{\partial\phi}{\partial r} - \frac{\partial\psi}{\partial r}\frac{\partial\phi}{\partial\theta} = \frac{r^2\sin\theta}{Re_1}D^2\phi, \tag{2}$$

$$2\xi\left[\cot\theta\frac{\partial\psi}{\partial r} - \frac{1}{r}\frac{\partial\psi}{\partial\theta}\right] - 2\phi\left[\cot\theta\frac{\partial\phi}{\partial r} - \frac{1}{r}\frac{\partial\phi}{\partial\theta}\right] - \left[\frac{\partial\psi}{\partial r}\frac{\partial\xi}{\partial\theta} - \frac{\partial\psi}{\partial\theta}\frac{\partial\xi}{\partial r}\right] = \frac{r^2\sin\theta}{Re_1}D^2\xi. \tag{3}$$

The streamfunction follows from the Poisson equation

$$-D^2\psi - \xi = 0, \tag{4}$$

where the differential operator is

$$D^2 = \frac{\partial^2}{\partial r^2} + \frac{1}{r^2}\frac{\partial^2}{\partial\theta^2} - \frac{\cot\theta}{r^2}\frac{\partial}{\partial\theta}. \tag{5}$$

α is defined as $\alpha = R_2/R_1 = \sigma + 1$. η is the Reynolds numbers ratio defined as $\eta = Re_2/Re_1$.

The boundary conditions are 'no slip' conditions at the spheres

$$\begin{aligned} &\phi(1,\ \theta) = \sin^2\theta, && \phi(\alpha,\ \theta) = \eta\sin^2\theta,\\ &\psi(1,\ \theta) = 0, && \psi(\alpha,\ \theta) = 0,\\ &\xi(1,\ \theta) = -\psi_{rr}, && \xi\alpha,\ \theta) = -\psi_{rr}. \end{aligned} \tag{6}$$

The symmetry conditions at the poles are

$$\begin{aligned} &\phi(r,\ 0) = 0, && \phi(r,\ \pi) = 0,\\ &\psi(r,\ 0) = 0, && \psi(r,\ \pi) = 0,\\ &\xi(r,\ 0) = 0, && \xi(r,\ \pi) = 0. \end{aligned} \tag{7}$$

There are no physical conditions for the vorticity function at the walls. Hence, Poisson equations are used:

$$\xi(1,\ \theta) + \psi_{rr}(1,\ \theta) = 0, \quad \xi(\alpha,\ \theta) + \psi_{rr}(\alpha,\ \theta) = 0. \tag{8}$$

The governing equations are discretized by central differences of second order and form a system of nonlinear algebraic equations:

$$G(X,\ Re_1,\ \eta) = 0, \tag{9a}$$

where X is the solution vector. The solution of system (9a) is a two-dimensional surface in real space $\Re^{N+1}$. Parts of this surface are calculated by determining its intersections with hyperplanes $Re_1 = \text{const.}$ or $\eta = \text{const.}$, i.e. by computing solution curves of

$$G(X,\ Re_1 = \text{const.},\ \eta) = 0, \qquad G(X,\ Re_1,\ \eta = \text{const.}) = 0. \tag{9b}$$

The folds of the surface are calculated as well.

Because the problems both depend only on one parameter, they can be abbreviated as

$$G(X,\ \lambda) = 0, \tag{9c}$$

where λ stands for the *Reynolds* number of inner sphere (Re_1) or Reynolds numbers ratio (η). This gives a sequence of iteration $[X^{(\upsilon)}(\lambda)]$ defined by

$$X^{(0)}(\lambda) \equiv \textit{initial estimate,} \tag{10a}$$

$$G_X(X^{(\upsilon)},\ \lambda)\left[X^{(\upsilon+1)} - X^{(\upsilon)}\right] = -G(X^{(\upsilon)},\ \lambda), \qquad \upsilon = 0,\ 1,\ 2\ldots \tag{10b}$$

Here G_X is the Jacobian matrix of (9c). One way to obtain good initial estimates is to use a Taylor expansion of the solution with respect to the changes in the parameter λ. Thus we use

$$X^{(0)}(\lambda + \delta\lambda) = X(\lambda) + \delta\lambda X_\lambda(\lambda). \tag{11a}$$

To obtain X_λ, we can use (9a) and it satisfies

$$G_X(X,\ \lambda)X_\lambda = -G_\lambda(X,\ \lambda). \tag{11b}$$

The method described in (10) and (11) is known as the Euler–Newton continuation. It is extremely effective and usually converges quadratically. However, it fails in points where the Jacobian matrix $G_X(X,\ \lambda) = 0$ is singular. To avoid the singular points, Keller's (1977) continuation method is introduced:

$$N(X(s,\ \lambda(s))) \equiv \left\langle \dot{X}(s_0)\cdot[X(s) - X(s_0)]\right\rangle + \dot{\lambda}(s_0)[\lambda(s) - \lambda(s_0)] - (s - s_0) = 0. \tag{12}$$

Here $[X(s_0,\ \lambda(s_0))]$ is a previously computed solution for λ fixed in the present discussion and $s = s_0$. $\dot{X} = \mathrm{d}X/\mathrm{d}s$ and $\dot{\lambda} = \mathrm{d}\lambda/\mathrm{d}s$ denote the components of a tangent vector to the solution path $[X(s),\ \lambda(s)]$. Then a new system of equations is written as

$$\begin{cases} G(X,\ \lambda) = 0, \\ N(X,\ \lambda,\ s) = 0, \end{cases}$$

which can be solved. The Jacobian of this new system is

$$\frac{\partial(G,\ N)}{\partial(X,\ \lambda)} = \begin{pmatrix} G_X & G_\lambda \\ N_X & N_\lambda \end{pmatrix}. \tag{13}$$

With the Euler–Newton continuation in s rather than λ, it is possible to follow the solution around singular points.

The singular points can be located at the place where the sign of the determinant of the Jacobian matrix changes. In doing so, it is necessary to use a great deal of computer memory storage and CPU time to calculate these singular points which may suffer from scaling problems in numerics. To reduce computer costs and avoid the scaling problems, we introduce a test function, $\Gamma_{i,j}(X,\ \lambda)$, proposed by Seydel (1988), shown as follows:

$$\Gamma_{i,j}(X,\ \lambda) = e_i^T \tilde{J}(X,\ \lambda)h, \tag{14}$$

where $\boldsymbol{h}$ satisfies the system

$$h = \tilde{J}_{i,j}^{-1} e_i, \tag{15}$$

e_i is a unit column vector and the matrix $\tilde{J}_{i,j}$ is reduced to $\tilde{J}$ by replacing its ith row by a unit base vector, i.e. $\tilde{J}_{i,j} \equiv \left[(I - e_i e_i^T)\tilde{J} + e_i e_j^T\right]$. Equation (15) guarantes that the column vector $\boldsymbol{h}$ is a nontrivial solution. The value of (14), $\Gamma_{i,j}(X,\ \lambda)$, approaches zero if $G_X(X,\ \lambda)$ approaches singular points. The quantity $\Gamma_{i,j}(X,\ \lambda)$ measures the rank-deficiency and serves as a test function. Therefore, the singular points can be determined

by monitoring the value of the test function. If the sign of the test function changes, a flow mode variation is encountered. However, $\Gamma_{i,j}(X,\ \lambda)$ is not singular at simple turning points. Detecting turning points is much easier through the sign change of $\partial\lambda/\partial s$. Other test functions may also be used for detecting bifurcation points. The most direct one is by zero leading eigenvalues, but it is much more time-consuming and thus less efficient for large problems.

To investigate the stability of various flow states obtained by the continuation method described above, a linear stability analysis is carried out. A basic state X_0 found by Newton's method during continuation is perturbed by small time-dependent quantities,

$$X = X_0 + \varepsilon\, \mathrm{e}^{\gamma t}, \tag{16}$$

where ε is a small disturbance vector. For transient solutions, a set of time-dependent equations can be derived and written as

$$M(X)\frac{\mathrm{d}X}{\mathrm{d}t} = G(X,\ \lambda), \tag{17}$$

where $M(X)$ is the mass matrix and it is singular because some equations, e.g. the stream equations, do not have an explicit time-dependent term. Substituting (16) into (17), after collecting the linear terms of ε, leads to the generalized algebraic eigenvalue problem:

$$\gamma M(X_0)\varepsilon = \tilde{J}(X_0)\varepsilon. \tag{18}$$

The matrix $\tilde{J}$ represents the Jacobian matrix of $G(X,\ \lambda)$ evaluated for the basic state solution. The stability of the basic state X_0 can be determined by the sign of the eigenvalue γ. The basic solution is infinitesimally stable if $Re\{\gamma\} < 0$ holds for all eigenvalues γ, i.e. if all perturbations in (16) will decay with time. If there is at least one eigenvalue with $Re\{\gamma\} > 0$, the corresponding eigenmode will grow as $t \to \infty$ and the basic solution is unstable. However, if the solution is already unstable, the sign change of $\det\{J\}$ alone does not give sufficient information about an exchange of stability. For this reason, it is necessary to calculate at least the leading eigenvalue, and this reduces the effort of the stability analysis significantly. However, because M is singular, some eigenvalues are infinite and they are not responsible for the linear instability. It is necessary to remove these infinite eigenvalues when calculating the leading eigenvalues. An effective algorithm for this purpose is a shift-and-inverse operation (Arnoldi algorithm). The generalized eigenvalue problem (18) is transformed into a standard eigenvalue problem:

$$\left(\tilde{J} - \beta M\right)^{-1} M\varepsilon = \hat{\gamma}\varepsilon, \qquad \hat{\gamma} = \frac{1}{\gamma - \beta}, \tag{19}$$

where β is a complex shift parameter such that $(\tilde{J} - \beta M)^{-1}M$ is not singular. This standard problem is then solved by a restarted, iterative Arnoldi method which is essentially a sophisticated extension of the power iteration method and allows a number of eigenvalues $\hat{\gamma}$ of largest magnitude to be calculated (Saad, 1992). ***ARPACK*** (Sorensen, 1992), an Arnoldi-method-based package, is then used to calculate the leading eigenvalues and corresponding eigenvectors. Real shift values are found satisfactory in the present study. The onset of instability in our calculation, where the leading eigenvalue becomes positive, is consistent with the bifurcation diagram or the test function.

3. Results and Discussion

3.1. Inner Sphere Rotating and Outer Sphere Stationary

The computational domain is discretized into equally spaced grid points in both the radial and the meridional direction. In order to determine the dependency of the numerical solution on the grid point distribution, three different grid structures are chosen for the investigation, i.e. 31×301, 41×301, and 41×361 (in the radial and the meridional direction, respectively). For the cases of $\sigma = 0.18$ and $\sigma = 0.176$, several numerical and experimental investigations are available in published literature. Table 1 provides a comparison of the current results with those of Marcus and Tuckerman (1987), Schrauf (1986), Bar-Yoseph *et al*. (1990), Bartels

Table 1. Critical Reynolds numbers (Re_{1c}) for the transition from a flow with m vortex pairs to a flow with n vortex pairs when $Re_2 = 0$ (— indicates that the data is not reported).

	σ	$0 \to 1$	$1 \to 0$	Hysteresis (ΔRe)	$0 \to 2$
		Numerical results			
This study					
(31×301)	0.18	650.23	643.6	6.63	745.7/790[c]
(41×301)	0.18	649.13	642.32	6.81	745.1/789
(41×361)	0.18	649.13	642.32	6.81	744.3/788
Marcus and Tuckerman	0.18	652.11	644.25	7.86	739.8/775
Schrauf	0.18	659.97	–	–	–
Schrauf[a]	0.176	–	652.89	–	750.01
Schrauf[b]	0.176	666.32	660.87	5.45	–
Bar-Yoseph	0.176	–	$665 - 657$	–	–
	0.18	666	–	–	753
Bartels	0.176	–	666.5	–	$728 - 776.5$
		Experimental results			
Wimmer	0.18	$649.5 - 653.4$	$624.6 - 653$	–	$800 - 810.6$

[a] Taken from the values listed in Marcus and Tuckerman (1987).
[b] Taken from the values listed in Bar-Yoseph *et al.* (1990).
[c] The first value is the Reynolds number that the 2-vortex flow starts to appear and the second value is the Reynolds number where the flow bifurcation is detected.

(1982), and Wimmer (1976). The present solutions may be regarded as grid-independent when the 41×401 grid system is used. As shown in Table 1, there is good agreement between the critical Reynolds numbers computed in the current study and the results reported previously.

3.1.1. Solution States

Figure 1 depicts the seven steady flow modes predicted in this study for a gap of $\sigma = 0.18$. The flow modes, shown in Figure 1(a)–(d), have been reported in previous literature and are referred to as 0-*vortex*, 0-*vortex with pinches*, 1-*vortex,* and 2-*vortex flow*, respectively. The other three flow modes are reported for the first time in this study. For purposes of simplicity, the domain is represented as rectangular, although in reality it is actually curved. Contours of $\Psi r \sin \Theta$, which are tangent to the meridional velocity, are plotted. The solid curves designate counter-clockwise circulation, while the dashed curves indicate clockwise circulation. In these flows, the Ekman pumping effect causes fluid to be thrown outward centrifugally along the rotating inner sphere and pulled away from the center of the stationary outer sphere. This results in a large-scale meridional flow whose direction is counter-clockwise in the northern hemisphere, and clockwise in the southern hemisphere. This phenomenon can be seen in all flows with non-zero Reynolds numbers.

Figure 1(e) is similar to Figure 1(c) in that it also contains one pair of Taylor vortices near the equator. However, its vortex size and strength are much smaller and weaker than those in Figure 1(c). The *asymmetric* 2-*vortex* state shown at $Re = 800$ in Figure 1(f) consists of two pairs of Taylor vortices, one of which is just slightly larger than the other and straddles the equator. Figure 1(g) predicts the occurrence of an *asymmetric* 1-*vortex with a pinch* flow mode when $Re = 1000$ and shows that it contains two Taylor vortices, one of which is larger and straddles the equator. It will be noted that this flow mode is characterized by a pinch on only one of the large-scale recirculations.

3.1.2. Bifurcation Diagram with Inner Sphere Rotating and Outer Sphere Stationary

Figure 2(a) presents the torque distributions of the different flow states which occur when the inner sphere rotates and the outer sphere remains stationary. It can be seen that there is reasonably good agreement between the solutions of the stable branches and the numerical results provided by Marcus and Tuckerman (1987). A schematic representation of the bifurcation diagram is shown in Figure 2(b), in which

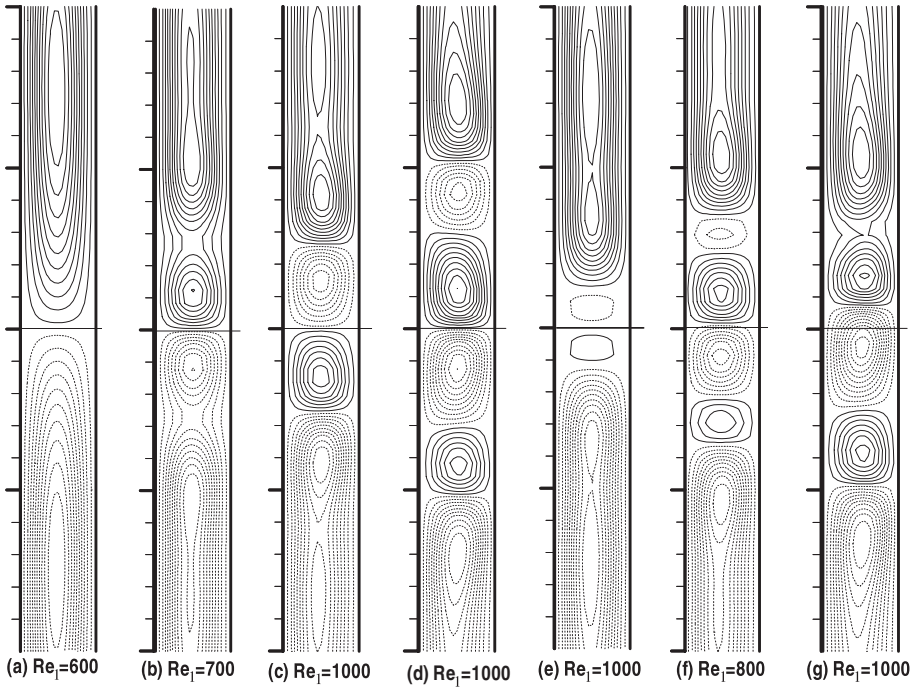

Figure 1. The seven steady flow modes predicted for $\sigma = 0.18$ in the case of rotation of the inner sphere and a stationary outer sphere. — marks the location of the equator.

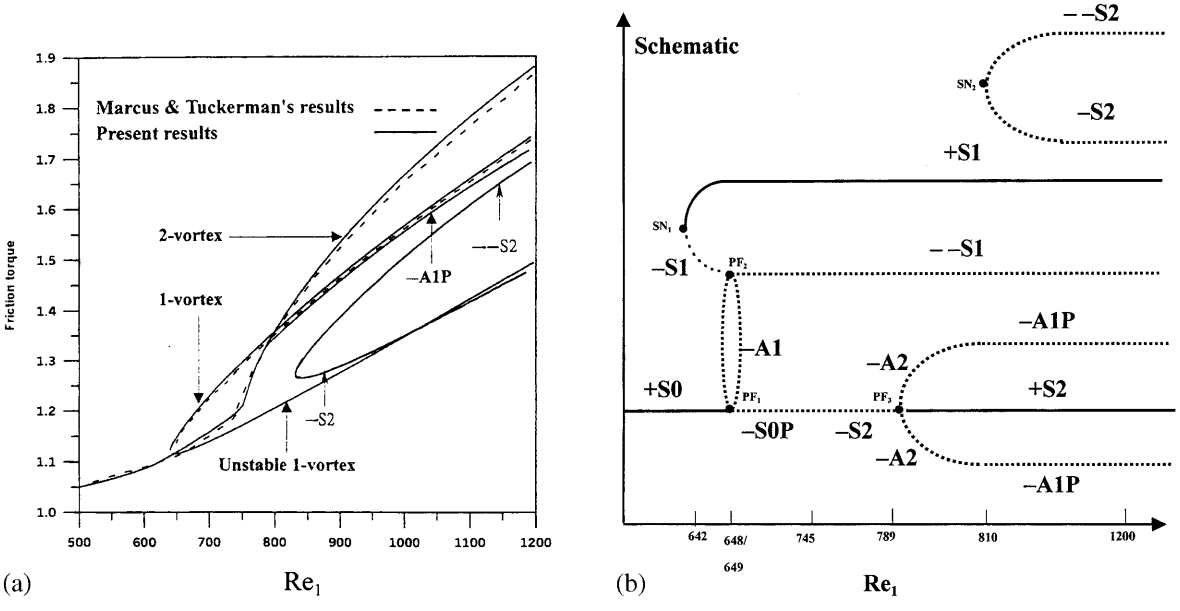

Figure 2. (a) Torque distributions of different states in the case of rotation of the inner sphere and a stationary outer sphere. (b) Schematic bifurcation diagram for $Re_1 < 1200$ in the case of rotation of the inner sphere and a stationary outer sphere. Note that the solution branch ($-$S2, SN$_2$, $--$S2) which is unconnected to the known branch can be calculated using the two-parameter continuation method described in this current study.

the vertical axis represents flow states and is neither a monotonic nor even a single-valued function of torque. Figure 2(a) labels the stable (solid lines) and unstable (dashed lines) branches with indices of $+$ and $-$, respectively. The character of the indices is determined from linear stability analysis of the eigenvalues of the Jacobian matrix. The second index of each label indicates the nature of symmetry of that

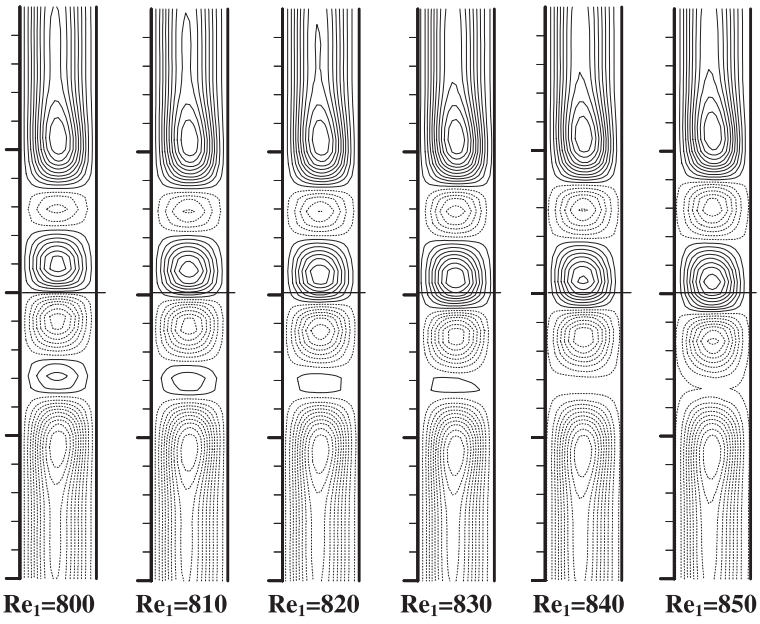

Figure 3. A sequence of steady states for different Reynolds number Re_1, ranging from asymmetric 2- to 1-vortex with pinches state. — marks the location of the equator.

branch, i.e. symmetric branches are labeled **S**, and asymmetric branches are designated **A**. The third index of the labels is a numerical value which indicates the number of Taylor vortex pairs in the flow. Finally, the fourth index, **P**, indicates whether or not the flow state possesses pinches in its large-scale recirculation.

It can be seen from Figure 2(b) that the 0-*vortex* with pinches (−S0P) gradually becomes an unstable 2-*vortex* flow (−S2) as Re_1 increases. By means of the linear stability analysis described in Section 2, it can be shown that the flow in the range $649 < Re_1 < 789$ is unstable, with a single unstable eigenmode. It is noted that there is no bifurcation between PF_1 and PF_3. This result is consistent with the test function approach. The unstable 2-*vortex* flow undergoes another subcritical pitchfork bifurcation (PF_3) at $Re_1 = 789$. This leads to a newly identified unstable *asymmetric* 2-*vortex* flow (−A2), whose asymmetry increases along its branch. The new branch bifurcates subcritically, which means that it inherits the stability index of the less stable portion of its parent branch. Considering the parent branch, as the flow mode gradually changes from −S0P to +S2 for increasing Re_1, a newly born vortex appears between a large basic recirculation and a Taylor vortex on each side of the equator. This newly born vortex gains in size and strength as Re_1 increases before finally settling to a stable 2-vortex flow.

Along each unstable asymmetric 2-*vortex* branch (−A2), the flow gradually transforms into an unstable *asymmetric* 1-*vortex with pinches* state (−A1P), which is identified for the first time in this study. Figure 3 shows the flow mode variation along the branch from −A2 to −A1P. With an increase in Re_1, it can be seen that the southern vortex near the large basic recirculation shrinks, and that the corresponding northern vortex grows in size and strength. Eventually, the southern large basic recirculation and the Taylor vortex merge to form a single pinched large basic vortex. Linear stability analysis reveals the existence of just one unstable mode in this range.

This study identifies for the first time the existence of a pair of unstable 2-vortex branches, which are created at $Re_1 = 810$ by a saddle-node bifurcation (SN_2). One of the branches is characterized by a positive eigenvalue, corresponding to the anti-reflection symmetric eigenmode. The flow along this branch destabilizes further, and becomes a twice unstable state (− −S2) with two eigenvectors of positive eigenvalues. It is interesting to note that SN_2 is unconnected to any of the previous solution branches. In general, the continuation method can only guarantee finding branches which are connected to known branches. However, this paper demonstrates that it is possible to obtain SN_2 solutions for two-sphere rotation. This issue will be discussed in greater detail later.

3.2. Bifurcation Diagram for Two Concentric Rotating Spheres

This section of the paper considers the case where the outer sphere rotates in addition to the inner one. Different Reynolds numbers (Re_1 and Re_2) of the two spheres generate different flow bifurcation diagrams and different existence ranges of Taylor vortex modes. Figures 4–7 present the appropriate flow diagrams as functions of Re_1 and Re_2. Within the range $638 < Re_1 < 745$, the bifurcation diagrams form closed curves. This is demonstrated in Figure 4(a), which presents the particular case where $Re_1 = 675$. (Note that friction torque is used as a measurement.) For the sake of clarity, a schematic diagram is also plotted, and is shown in Figure 4(b). When the outer sphere is stationary (i.e. $Re_2 = 0$) and the inner one rotates at angular velocities within the specified range, it is seen that there are three modes, namely stable 1-, unstable 1-, and 0-vortex with pinches state. Note that $Re_2 > 0$ indicates co-rotation of the spheres, while $Re_2 < 0$ denotes counter-rotating cases. In this bifurcation diagram, the stable 1-vortex state exists between two saddle-node bifurcations (SN_1 and SN_2). Additionally, the flow state (+S1) is destabilized by these two saddle-node bifurcations, and becomes an unstable 1-vortex state (−S1) with a positive unstable eigenvalue, which corresponds to an anti-reflection symmetric eigenmode. Following the −S1 flow further reveals the existence of two pitchfork bifurcations (PF_1 and PF_2) in both the co-rotating and the counter-rotating spheres cases. For both PF_1 and PF_2, the −S1 flow may follow one of two routes, namely (1) the flow may become an unstable 0-vortex with pinches state (−S0P) via a symmetry-breaking transition, or (2) the flow may destabilize further and become the twice unstable 1-vortex state (−S1). These branches connect the two pitchfork bifurcations (PF_1 and PF_2) and close the curve of the bifurcation diagram.

When $745 < Re_1 < 782$, the bifurcation diagrams still form closed curves and are all similar to Figure 5(a), which presents the case at $Re_1 = 770$. The corresponding schematic diagram is depicted in Figure 5(b). It can be seen that the bifurcation diagrams for both co- and counter-rotating spheres in this Re_1 range are broadly similar to those in $638 < Re_1 < 745$. However, the unstable 0-vortex with pinches branch is slightly different than that which is observed in the previous diagram, namely a new pair of saddle-node bifurcations (SN_3 and SN_4) appear. The basic flow has two vortices near these saddle-node bifurcations. The vortex flows may be one of two types; an unstable 2-vortex state (−S2) or a twice unstable state (− −S2). The unstable 2-vortex state located at $Re_2 = 0$ corresponds to the unstable 2-vortex state (−S2) shown in Figure 2.

When $782 < Re_1 < 836$, the bifurcation diagrams still form closed curves and are all similar to Figure 6(a), which shows the case at $Re_1 = 830$. The corresponding schematic diagram is given in Figure 6(b). These bifurcation diagrams are also similar to those in the range $745 < Re_1 < 782$, other than along the

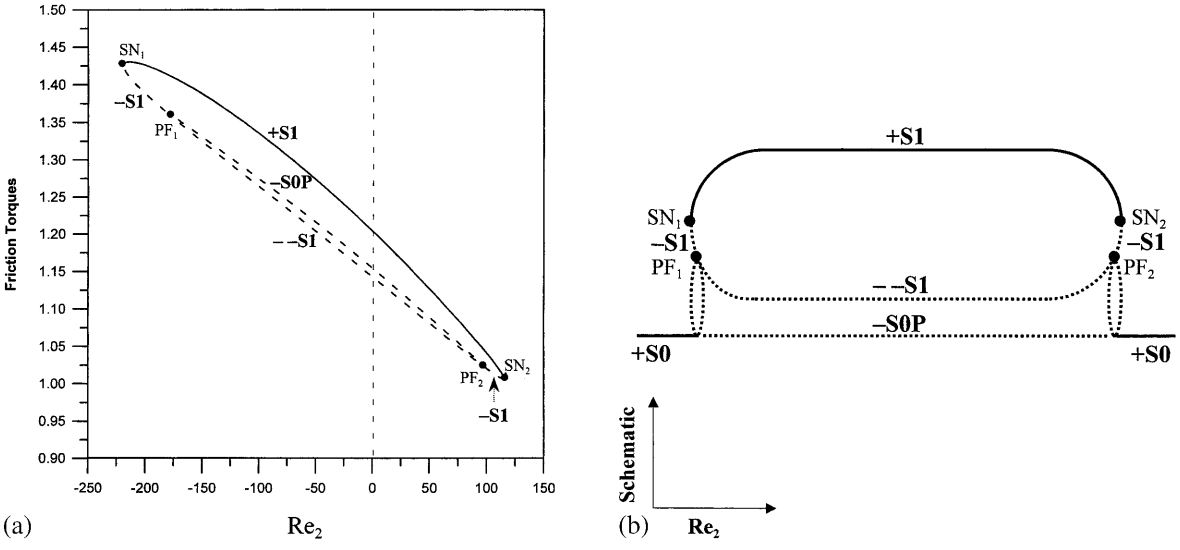

Figure 4. (a) Bifurcation diagram for co-/counter-rotating spheres in the range $638 < Re_1 < 745$. Stable and unstable flows are indicated by solid and dashed lines, respectively. Saddle-node bifurcations and pitchfork bifurcations are represented by circular solid points. (b) Schematic bifurcation diagram of (a).

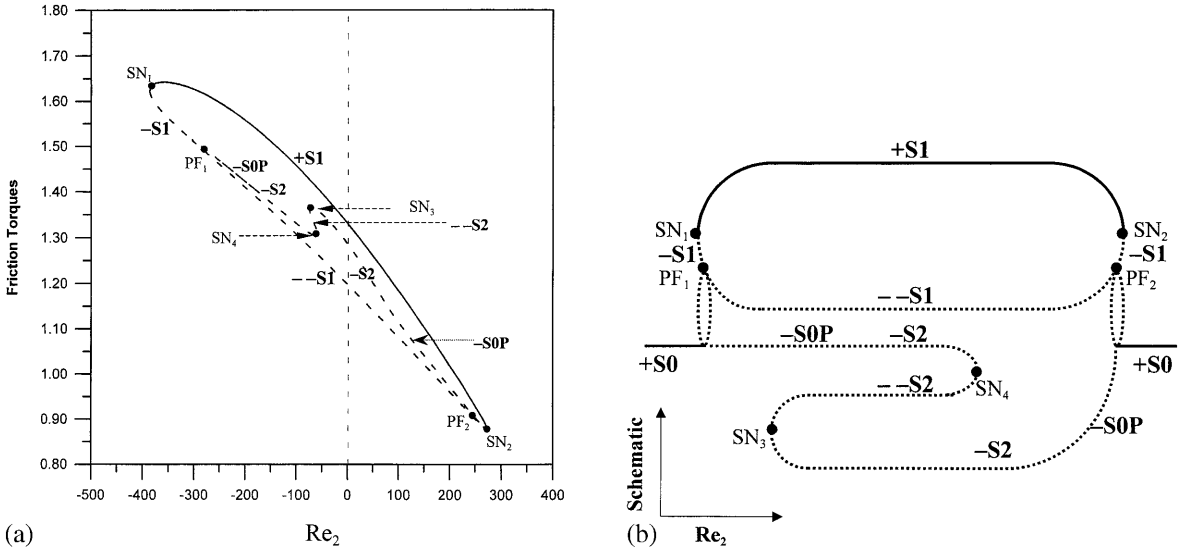

Figure 5. (a) Bifurcation diagram for co-/counter-rotating spheres in the range $745 < Re_1 < 782$. Stable and unstable flows are indicated by solid and dashed lines, respectively. Saddle-node bifurcations and pitchfork bifurcations are represented by circular solid points. (b) Schematic bifurcation diagram of (a).

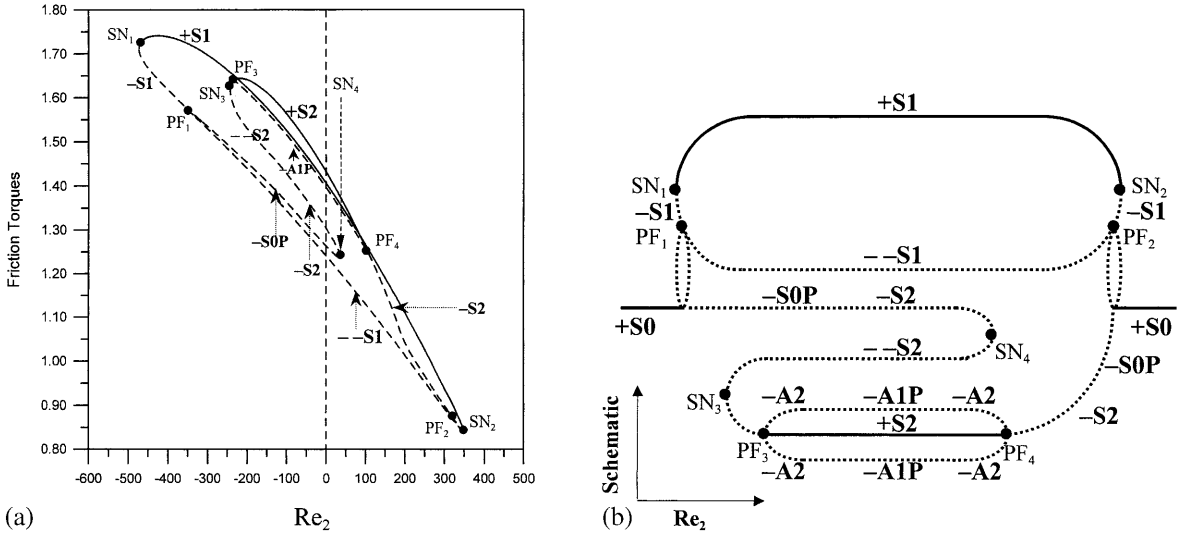

Figure 6. (a) Bifurcation diagram for co-/counter-rotating spheres in the range $782 < Re_1 < 836$. Stable and unstable flows are indicated by solid and dashed lines, respectively. Saddle-node bifurcations and pitchfork bifurcations are represented by circular solid points. (b) Schematic bifurcation diagram of (a).

branch with two saddle-node bifurcations. The flow mode is an unstable 0-vortex with pinches state undergoing a pitchfork bifurcation PF_1. After passing through a saddle-node bifurcation (SN_3), the flow gradually becomes an unstable 2-vortex flow with one unstable anti-reflection symmetric eigenmode. This unstable 2-vortex flow may then undergo another subcritical pitchfork bifurcation (PF_3), leading to a pair of unstable asymmetric 2-vortex flows. Additionally, the flow may also restabilize at this subcritical pitchfork bifurcation and become a stable 2-vortex flow (+S2) along the continuation path. During this Re_2-dependent evolution, the stable 2-vortex state located at $Re_2 = 0$ corresponds to the stable 2-vortex state (+S2) shown in Figure 2. Proceeding further along this branch, the stable 2-vortex flow is destabilized via another subcritical pitchfork bifurcation (PF_4) and returns to the unstable 2-vortex state (−S2). Two asymmetric branches with one positive leading eigenvalue, corresponding to an anti-symmetric eigenvector, connect the two subcritical pitchfork bifurcations (PF_3, PF_4). Along these two branches, the flow gradually evolves from unstable asym-

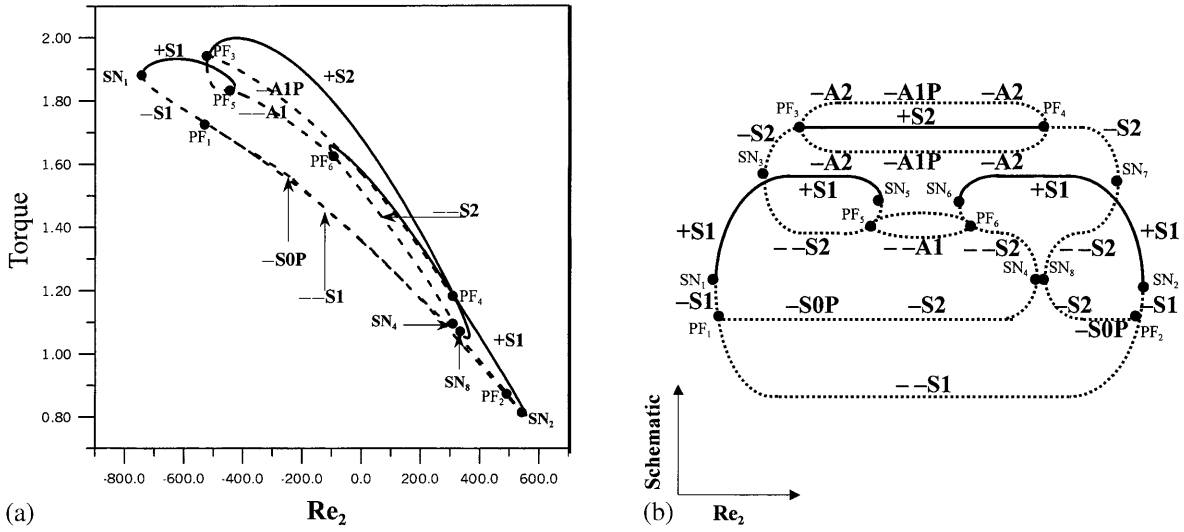

Figure 7. (a) Bifurcation diagram for co-/counter-rotating spheres for $Re_1 = 1000$ and $-500 < Re_2 < 400$. Stable and unstable flows are indicated by solid and dashed lines, respectively. Saddle-node bifurcations and pitchfork bifurcations are represented by circular solid points. (b) Schematic bifurcation diagram of (a).

metric 2-vortex to asymmetric 1-vortex with pinches state (−A1P), before finally returning to the unstable asymmetric 2-vortex state once again. The unstable asymmetric states located at $Re_2 = 0$ on these branches correspond to the unstable asymmetric state in Figure 2. Note that the crossings of the +S1 branch near PF_3 and PF_4 in the torque diagram do not represent bifurcations.

For a gap ratio of $\sigma = 0.154$ and the case of inner sphere rotation with a stationary outer sphere, a stable asymmetric 1-vortex solution exists in the bifurcation diagram (Mamun and Tuckerman, 1995). It is of interest to determine whether this same solution would be manifest in the current case of two rotating spheres and a gap of $\sigma = 0.18$. Calculations were carried out for higher values of Reynolds number. It was found that when $Re_1 > 950$, a twice unstable asymmetric 1-vortex solution (− −A1) appears in the case of counter-rotating spheres. When $Re_1 = 1000$ and $-500 < Re_2 < 400$, the bifurcation diagram forms a closed curve. The corresponding schematic diagram is given in Figure 7. The 1-vortex branch is separated into two distinct 1-vortex branches by the two saddle-node bifurcations, i.e. SN_5 and SN_6, and the flow states become the unstable 1-vortex states with one unstable reflection symmetric eigenmode, respectively. Proceeding further along these two distinct branches, it can be seen that the flow states may respectively undergo two pitchfork bifurcations (PF_5, PF_6), leading to a pair of unstable asymmetric 1-vortex flows (− −A1) and two twice unstable 2-vortex flows (− −S2). The asymmetric 1-vortex branches possess a pair of conjugate leading eigenvalues, corresponding to an anti-symmetric eigenvector and a symmetric eigenvector, and connect the two pitchfork bifurcations (PF_5, PF_6). For the parameter values under current consideration, the asymmetric solution (− −A1) is unstable. However, as noted above, a stable asymmetric 1-vortex solution exists in the bifurcation diagram when the gap ratio $\sigma = 0.15$ and the inner sphere rotates but the outer sphere is stationary. Figure 7 sheds important new light on the origination of the asymmetric solution. Whether the asymmetric 1-vortex solution is stable or unstable would appear to depend on the value of the gap ratio, i.e. existence of a stable flow may be determined by a critical gap ratio. However, establishing the value of this critical gap is not within the scope of this study.

3.3. Linear Stability Analysis in Differential Rotating Spheres

The numerical methods described in Section 2 can be used to calculate the leading eigenvalues and corresponding eigenmodes for each solution branch. The leading eigenvalues on each branch in this study are always real. Figure 8 shows the computed eigenvalue λ of the most unstable eigenmode as a function of Re_2 along the branch from SN_4 to PF_4 in the bifurcation diagram where $Re_1 = 840$. Since the Navier–Stokes equations are adopted and the boundary conditions are associated with spherical Couette flow which

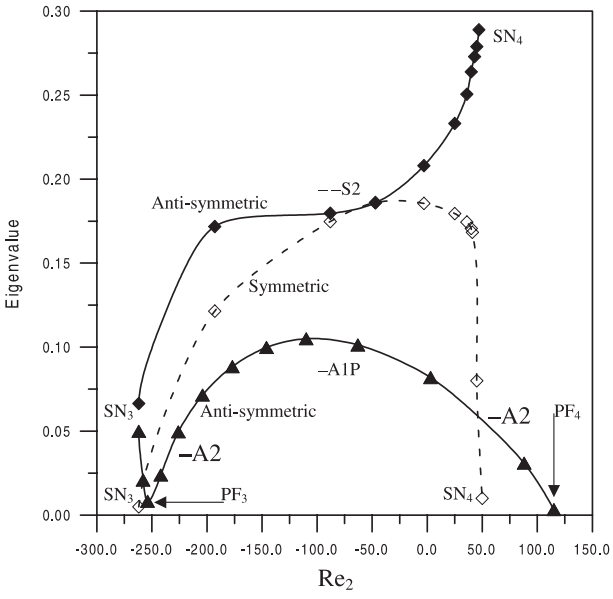

Figure 8. Eigenvalue distributions as a function of Re_2.

are all reflection symmetric, then the linear eigenmodes of the equilibrium must be either reflection or anti-reflection symmetric. In Figure 6(b), there is only one positive eigenvalue, corresponding to the anti-reflection symmetric eigenmode, from PF_1 along the −S2 branch. Proceeding further along this branch, after passing through SN_4 at $Re_2 = 41$, the flow destabilizes further, and an additional positive eigenvalue appears, as indicated by the hollow rhombic symbols and dashed lines in Figure 8. This eigenvalue corresponds to the reflection symmetric eigenmode. The original positive eigenvalues are represented by solid rhombic symbols and connected by solid lines. Therefore, it can be seen that there are two eigenvectors with positive eigenvalues connecting SN_4 to the saddle-node bifurcation (SN_3). The corresponding reflection and anti-reflection symmetric eigenvectors of the twice unstable 2-vortex flow (− −S2) at $Re_1 = 830$ and $Re_2 = -88$

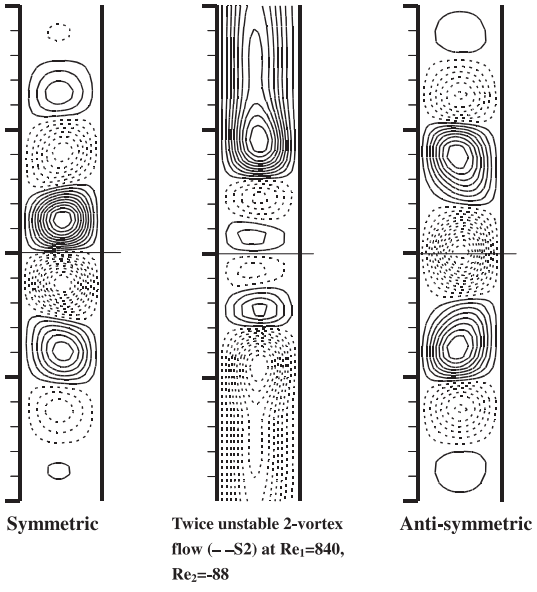

Figure 9. Corresponding reflection and anti-reflection symmetric eigenvalues of the twice unstable 2-vortex flow (−−S2) at $Re_1 = 830$ and $Re_2 = -88$. — marks the location of the equator.

are shown in Figure 9. The eigenvalues gradually reduce their magnitudes as Re_2 decreases after SN_4 along the anti-reflection symmetric branch. After passing through SN_3, the positive eigenvalue corresponding to the reflection symmetric eigenmode changes sign, i.e. at $Re_2 = -265$. The other positive eigenvalues, indicated by the solid triangular symbols and lines in Figure 8, undergo another subcritical pitchfork bifurcation (PF_3) at $Re_2 = -255$, i.e. very close to SN_3. As seen in Figure 6(b), PF_3 has two unstable asymmetric solution branches. Along these two asymmetric branches (from $-$A2 to $-$A1P equilibrium), there exists one positive eigenvalue corresponding to the anti-reflection symmetric eigenmode, which is also indicated by solid triangular symbols and lines in Figure 8. With increasing Re_2, the magnitudes of both asymmetry and eigenvalue increase and attain maximum values at approximately $Re_2 = -100$. As Re_2 continues to increase beyond this value, both magnitudes gradually decrease.

3.4. Torque Distributions in Two Concentric Rotating Spheres

Although it is possible to construct a three-dimensional diagram to show torque distributions as functions of Re_1 and Re_2, this paper prefers to use two-dimensional diagrams in order to depict the computed results more clearly. As discussed previously, Figure 2(a) shows the computed torque distributions for different solution branches in the case of inner sphere rotation with a stationary outer sphere. The solution branches ($-$S2 and $--$S2), which are unconnected to the primary solution branch ($+$S2), are clearly visible.

For the case of two concentric rotating spheres, Figure 10 shows the distributions of the critical Reynolds numbers (Re_{2c}) of various flow modes as a function of Re_1. Re_{2c} is defined as the existence range of stable 1-vortex flow for either co-rotating or counter-rotating spheres. The distributions of these critical numbers form a parabolic curve, and the distribution of the largest friction torque for the stable 1-vortex is denoted by the dashed line. Taylor vortices exist inside the curve, while outside the curve only basic flow exists. As Re_1 increases, the existence range of Taylor vortices gradually expands, and the number of flow modes which exist within the range also increases. For larger values of Re_1, the Taylor vortices are more coherent, and so it takes more angular momentum flux of the outer sphere to destabilize the flow modes in both the co-rotating and the counter-rotating cases. Furthermore, for any specific angular velocity of the inner sphere, the absolute value of the critical number (Re_{2c}) is always larger in the case of counter-rotation. Hence, more angular

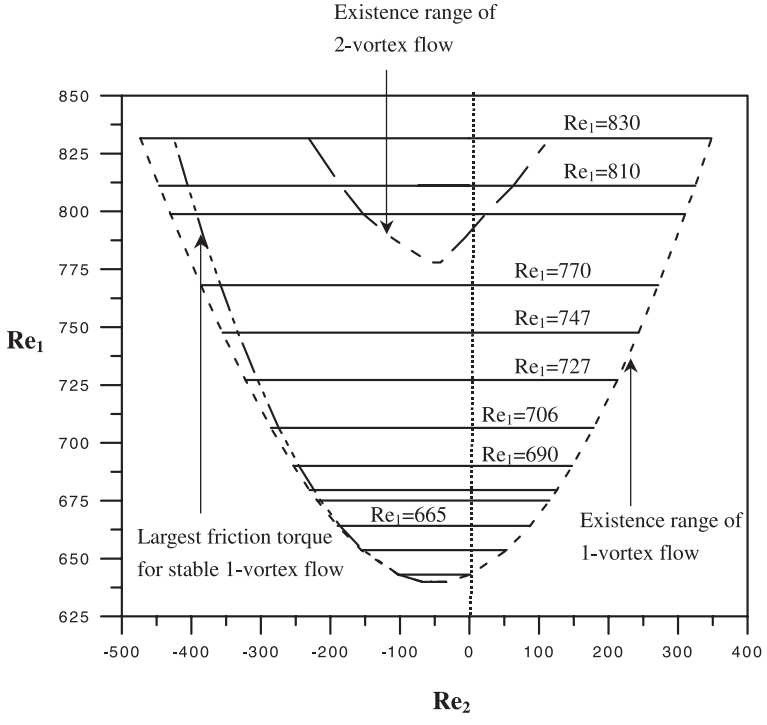

Figure 10. Instability region shown as functions of Re_1 and Re_2.

momentum flux is required before the flow destabilizes for counter-rotating spheres. Such phenomena are similar to those which occur in two coaxial rotating cylinders.

By controling the outer sphere rotation, it is possible to obtain the solution branch unconnected to the known solution branches which was identified in the case of a rotating inner sphere and a stationary outer sphere. At values of $Re_1 = 642$ and $Re_1 = 648$, the saddle-node bifurcation (SN_1) and the symmetry-breaking pitchfork bifurcation (PF_1) are located on the coordinate $Re_2 = 0$, correponding to the saddle-node bifurcation (SN_1) and the pitchfork bifurcation (PF_1) shown in Figure 2(b), respectively. As Re_1 is increased further, the range of critical Reynolds numbers (Re_{2c}) expands, and the flow states at $Re_2 = 0$ (including stable 1-vortex, unstable 1-vortex, and 0-vortex with pinches states) grow in strength and size. When $745 < Re_1 < 782$, two saddle-node bifurcations and a subsequent twice unstable 2-vortex state appear on the original 0-vortex with pinches branch. This phenomenon appears first in the counter-rotating condition when $Re_1 = 745$. With increasing Re_1, the range between the pitchfork bifurcations (PF_1, PF_2) and the existence range of the unstable 2-vortex state spread even wider. When $Re_1 > 745$, the unstable 2-vortex state is found on the coordinate of $Re_2 = 0$, which corresponds to state $-$S2 in Figure 2(b). For the range $782 < Re_1 < 836$, two subcritical pitchfork bifurcations (PF_3, PF_4) appear on the original 0-vortex with pinches state branch in addition to the two saddle-node bifurcations (SN_4 and SN_3). Two unstable asymmetric branches originate from PF_3 and PF_4, and the unstable 2-vortex flow also stabilizes via the two pitchfork bifurcations. The two subcritical pitchfork bifurcations and the two asymmetric branches ($-$A1P) appear first in the counter-rotating condition at $Re_2 = 782$. The existence range of these two pitchfork bifurcations (PF_3, PF_4) enlarges with increasing Re_1. At values of $Re_1 = 789$ and $Re_1 = 810$, PF_3 and SN_4 are located at the coordinate of $Re_2 = 0$, corresponding to PF_3 and **SN_2** in Figure 2(b), respectively. Moreover, when $Re_1 > 782$, the stable 2-vortex branch and the unstable asymmetric branch continue to appear on the coordinate of $Re_2 = 0$, corresponding to the branch $+$S2 and the branch $-$A1P in Figure 2(b). Also, when $Re_1 > 810$, the unstable 2-vortex branch and the twice unstable 2-vortex branch continue to appear on the coordinate of $Re_2 = 0$, and correspond to the branch $-$S2 and the branch $--$S2 in Figure 2(b). In Figure 10, for the transition from basic flow to 1-vortex flow, the lowest critical Re_{1c} occurs not at $Re_2 = 0$ and $Re_1 = 642$, but rather at $Re_2 = -80$ and $Re_1 = 638$. Therefore, by properly adjusting the angular velocity of the outer sphere in the counter-rotating condition, it is possible to sustain a stable Taylor vortex at a lower value of Re_1 than in the case of a stationary outer sphere. This may be explained by the fact that for counter-rotating spheres, the fluid is drawn onto the opposite azimuthal directions in the boundary layers of the two spheres, and this makes the Taylor vortices stronger and more coherent.

Figure 11 shows the stable 1-vortex states for corresponding values of Re_2. As Re_2 becomes strongly counter-rotating, it can be seen that another type of basic meridional flow appears, i.e. an additional elongated region of counter-circulation develops near the pole and the outer sphere in each hemisphere. This phenomenon is clearly visible in Figure 11, which shows the case for $Re_2 = -500$. Zikanov (1996) reported a similar flow structure although a different gap ratio was investigated in his paper. Furthermore, it takes more angular momentum flux to destabilize the 1-vortex flow. In direct contrast to the counter-rotating case, in the co-rotating case, the fluid is drawn onto the same azimuthal directions in the boundary layers. The strength of the Taylor vortices is therefore much weaker, and so it requires less angular momentum flux to destabilize the vortex. Accordingly, the absolute values of the critical Reynolds number Re_{2c} for counter-rotating spheres are much larger than those for co-rotating spheres for a specific value of Re_1.

3.5. Vortex Sizes for Different Vortex Modes for Two Concentric Rotating Spheres

Figure 12 shows the vortex-size of the 1-vortex state as a function of Re_1 and Re_2. It can be seen that for specific values of Re_1, the vortex-size distributions form closed curves. These curves are circular at low Re_1 values and become deformed circles as Re_1 increases. The upper and lower parts of the circles denote the stable and unstable 1-vortex states, respectively. When $Re_2 = 0$, increasing Re_1 results in the stable 1-vortex flow gradually growing in size, although the size of the unstable 1-vortex remains approximately constant. In counter-rotating conditions, the vortices in the flow grow in strength and size due to the interaction effect of the inner and outer sphere boundaries. Regardless of the absolute value of Re_1, the largest vortex-size of the stable 1-vortex state always occurs in the counter-rotating condition at an approximate location of

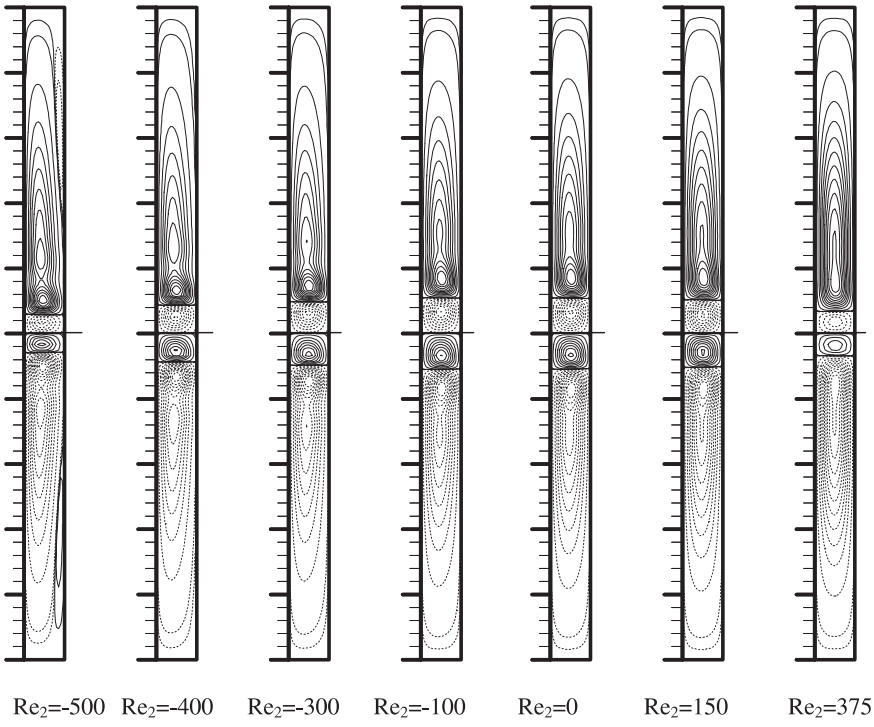

Figure 11. Stable 1-vortex states for corresponding values of Re_2 and a constant value of $Re_1 = 830$. As Re_2 becomes strongly counter-rotating, another type of basic meridional flow appears, i.e. an additional vortex develops near the pole and the outer sphere in each hemisphere. This is clearly visible in the case of $Re_2 = -500$. — marks the location of the equator.

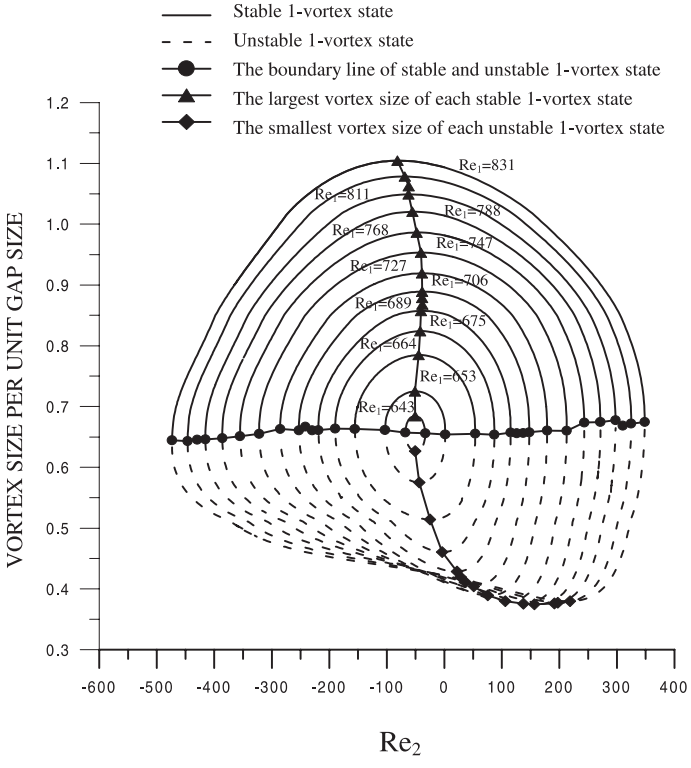

Figure 12. Vortex-size distributions of 1-vortex flow as functions of Re_1 and Re_2. Solid lines indicate the vortex-size distributions of the stable 1-vortex flow, while dashed lines indicate those of the unstable 1-vortex flow. The boundary line between the stable and unstable 1-vortex state is also shown.

$Re_2 = -50$. With decreasing Re_2, the counter-rotating and interaction effects in the azimuthal direction between the inner and outer sphere boundaries become more significant, and this in turn gradually causes the existing vortices to twist and lose their stability. In the co-rotating spheres condition, the interaction effect in the azimuthal direction between the inner and outer sphere boundaries gradually becomes weaker as Re_2 increases. This gradually causes the existing vortices to shrink in size and strength, and eventually to lose their stability. The smallest vortex-size of the unstable 1-vortex state occurs first in the counter-rotating condition at smaller values of Re_1. It is noted that the unstable vortex-size remains approximately constant for values of $Re_2 > 100$.

4. Conclusions

This paper has investigated the steady flow between co- and counter-rotating concentric spheres for a gap width of $\sigma = 0.18$. A continuation method was used to study the bifurcation structure and the instability of the flow using Navier–Stokes equations. The method used a test function to predict and locate singularities, in which a bifurcation was indicated by a zero quantity of the test function. The test function is continuous over a sufficiently large interval to be valid for the cases considered in this study, and the results confirm that the test function approach serves as an effective tool in the location of singular points. The computed solutions were carefully checked to be grid-independent, and show reasonably good agreement with numerical solutions and experimental data reported in available literature. The current study has clarified the instability regions of the two-dimensional flow.

In the condition where the inner sphere rotates and the outer remains stationary, three pitchfork bifurcation points, namely PF_1, PF_2, and PF_3, and two saddle-node bifurcation (SN_1 and SN_2) were detected. Previous studies identified the existence of the 0-, 1-, and 2-*vortex* flow modes. However, this current study has identified and investigated three additional steady states and solution branches, namely (1) the unstable *asymmetric* 2-*vortex* state ($-$A2, via a pitchfork bifurcation, PF_3), (2) the unstable *asymmetric* 1-*vortex with pinches* state ($-$A1P, subsequent to the $-$A2 state), and (3) a pair of unstable 2-vortex branches ($-$S2 and $--$S2, created by a saddle-node bifurcation, SN_2). The pair of unstable 2-vortex branches, which are independent of the primary branch, are reported for the first time in this study.

The continuation method can only guarantee identifying branches which are connected to known branches. However, the current study has demonstrated that by proper control of the rotation of the outer sphere, i.e. by imposing another continuation parameter on the system, solutions unconnected to the known branches can be located. In other words, some branches, which are independent of the primary known branch in a one-parameter system, can be identified through continuation of another parameter, and associated with the primary branches via a two-parameter system.

In the condition where both spheres rotate within the considered parameter range (i.e. $\sigma = 0.18$, $Re_1 < 1000$, and $-500 < Re_2 < 400$), this study identifies three stable steady flow modes ($+$S0, $+$S1, and $+$S2) and seven unstable steady flow modes ($-$S0P, $-$S2, $-$S1, $-$A2, $-$A1P, $-$S1, and $--$S2) with either one or two unstable eigenmodes. These states are connected to each other and form bifurcation structures. Different bifurcation diagrams in Re_1 and Re_2 are used to describe the relationships between these stable and unstable flow modes, and are useful tools in understanding the allowable transitions among stable states. All of the bifurcation diagrams produced in this study are broadly similar and all form closed curves. The study presents four bifurcation diagrams to describe the different bifurcation structures which occur at four distinct values of Re_1 in the range $Re_1 < 1000$. It is noted that a stable 1-vortex state always exists between the two saddle-node bifurcations shown in the bifurcation diagrams. From the sequential variations of bifurcation structure, it may be deduced that the existence of a stable 1-vortex state will be accompanied by both unstable 0-vortex with pinches states and 1-vortex states. The major differences between these bifurcation structures are the sequential variations along the branch of the 0-vortex with pinches state. The stable 2-vortex state appears on this branch at the final pitchfork bifurcation stage (PF_3 and PF_4). The study shows that the origin and development of stable 1- and 2-vortex states can be explained successfully using bifurcation theory.

For the case of 1-vortex flow with rotation of both spheres, it has been shown that the range of instability regimes gradually expands with increasing values of Re_1, and that it forms a parabolic curve. Flows within this range comprise various stable or unstable states. It has been found that the regimes for each mode always appear first in the counter-rotating case. Furthermore, for different values of Re_1, the friction torque of

each flow mode for the condition of counter-rotating spheres is always larger than in the case of co-rotating spheres. Also, the largest friction torque of the stable states always occurs in the counter-rotating condition because more angular momentum flux is required to destabilize the flow in these rotation conditions.

For specific values of Re_1, the vortex-size distributions of 1-vortex flow form closed curves. As Re_2 decreases, the counter-rotating and boundary interaction effects of the inner and outer spheres become more significant. This gradually causes the existing vortices to twist and to lose their stability. For the case of co-rotating spheres, the boundary interaction effects of the inner and outer spheres gradually become weaker as Re_2 increases. Thus, the existing vortices gradually shrink in size and strength and eventually lose their stability at a critical Reynolds number Re_{2c}. For specific values of Re_1, the largest vortex-size of the stable 1-vortex state always occurs in the counter-rotating condition.

Constructing a complete bifurcation diagram is useful in revealing the physics of a flow, and it was the intention of the authors to develop a comprehensive diagram within this study. The diagram can be used to reveal the location of stable solutions, and their relations to unstable solutions. For higher Reynolds number flows, the diagram may also be used to check dynamics responses to disturbances by considering flow transitions from laminar to turbulence. However, this involves the use of three-dimensional, transient, and accurate computations, which are beyond the present scope of this study.

Acknowledgment

We thank Professor Sorensen of Rice University for making ARPACK available.

References

Bartels, F. (1982). Taylor vortices between two concentric rotating spheres *J. Fluid Mech.*, **119**, 1–25.

Bar-Yoseph, P., Solan, A. R., Hillen K., and Roesner G. (1990). Taylor vortex flow between eccentric coaxial rotating spheres. *Phys. Fluids*, **2**(9), 1564–1573.

Bühler, K. (1990). Symmetric and asymmetric Taylor vortex flow in spherical gaps. *Acta Mechanica*, **81**, 3–38.

Keller, H.B. (1977). Numerical solution of bifurcation and nonlinear eigenvalue problems. In *Applications of Bifurcation Theory* (P. Rabinowitz, ed.), pp. 359–384. Academic Press, New York.

Luo, W.-J., and Yang, R.-J. (1998). Numerical simulation of a spherical Taylor–Couette flow bifurcation by a continuation method. In proceedings of the 16th *International Conference on Numerical Methods in Fluid dynamics* (C.H. Bruneau, ed.), pp. 195–200. Springer-Verlag, New York.

Mamun, C.K., and Tuckerman, L.S. (1995). Asymmetry and Hopf bifurcation in spherical Couette flow. *Phys. Fluids*, **7**(1), 80–91.

Marcus, P.S., and Turkerman, L.S. (1987). Simulation of flow between concentric rotating spheres, Part 1–steady states and Part 2–transitions. *J. Fluid Mech.*, **185**, 1–65.

Saad, Y. (1992). *Numerical Methods for Large Eigenvalues Problems*. Halsted press, New York.

Schrauf, G. (1986). The first instability in spherical Taylor–Couette flow. *J. Fluid Mech.*, **166**, 287–303.

Seydel, R. (1988). *From Equilibrium to Chaos: Practical Bifurcation and Stability Analysis*. Elsevier, New York.

Sorensen, D.C. (1992). Implicit application of polynomial filters in a *k*-step Arnoldi method, *SIAM J. Matrix Anal. Appl.*, **13**, 357–367.

Wimmer, M. (1976). Experiments on a viscous fluid flow between concentric rotating spheres. *J. Fluid Mech.*, **79**, 317–335.

Yang, R.-J. (1996). A numerical procedure for predicting multiple solutions of a spherical Taylor–Couette flow. *Int. J. Numer. Methods Fluids*, **22**, 1135–1147.

Yavorskaya, I.M., and Belyaev, Yu.N. (1986). Hydrodynamic stability in rotating spherical layers: application to dynamics of planetary atmospheres. *Acta Astro.*, **13**(6/7), 433–440.

Yavorskaya, I.M., Belyaev, Yu.N., and Monakhov, A.A. (1977). Stability investigations and secondary flows in rotating spherical layers at arbitrary Rossby number. *Sov. Phys. Dokl*. **22**, 717–719. (Transl. from *Dokl. Akad. Nauk SSSR* (1977), **237**, 804–807.)

Yavorskaya, I.M., Belyaev, Yu.N., Monakhov, A.A., Astafeva, N.M., Scherbakov, S.A., and Vvedenskaya, N.D. (1980). Stability, non-uniqueness and transition to turbulence in the flow between two rotating spheres. In *Theoretical and Applied Mechanics* (F.P.J. Rimrott and B. Tabarrok, eds.), pp. 431–443. North-Holland, Amsterdam.

Zikanov, O.Yu. (1996). Symmetry-breaking bifurcations in spherical Couette flow. *J. Fluid Mech.*, **310**, 293–324.